Inverse Designing Surface Curvatures by Deep Learning

Guo, Yaqi; Sharma, Saurav; Kumar, Siddhant

Inverse Designing Surface Curvatures by Deep Learning

Yaqi Guo, Saurav Sharma,* and Siddhant Kumar*

Smooth and curved microstructural topologies found in nature—from soap films to trabecular bone—have inspired several mimetic design spaces for architected metamaterials and bio-scaffolds. However, the design approaches so far are ad hoc, raising the challenge: how to systematically and efficiently inverse design such artificial microstructures with targeted topological features? Herein, surface curvature is explored as a design modality and a deep learning framework is presented to produce topologies with as-desired curvature profiles. The inverse design framework can generalize to diverse topological features such as tubular, membranous, and particulate features. Moreover, successful generalization beyond both the design and data space is demonstrated by inverse designing topologies that mimic the curvature profile of trabecular bone, spinodoid topologies, and periodic nodal surfaces for application in bio-scaffolds and implants. Lastly, curvature and mechanics are bridged by showing how topological curvature can be designed to promote mechanically beneficial stretching-dominated deformation over bending-dominated deformation.

1. Introduction

Nature is replete of porous structures with unique curvature topologies—from the simplest example of soap films with constant mean curvatures (Plateau's law[1,2]) to the morphogenesis-driven Turing patterns[3,4] in animal skin pigmentation; from biological systems such as trabecular bone[5–7] and vascular networks[8,9] to non-biological systems like porous ceramics, nanoporous gold,[10] and block copolymers[11] (see **Figure 1**). Driven by complex relaxation dynamics and nonequilibrium phenomena such as self-assembly,[12–14] pattern formation,[15–17] and phase ordering kinetics,[18,19] both understanding and tuning such physics behind the natural emergence of complex curvature topologies opens up new avenues for advances in materials engineering.

For instance, mimicking the microstructural curvature topologies of nanoporous gold and phase-separated block copolymers, spinodoid metamaterials[11,20–22] have sparked significant interest for their potential applications in bio-implants,[23] lightweight structures,[24] energy absorption,[25] mass transport,[26] and more. The microstructure of these materials emerges from a spinodal decomposition process (i.e., rapid separation of immiscible phases) via either self-assembly[11] or combination of in silico design and 3D printing.[21] In spinodal decomposition, the phase separation is governed by minimization of the bulk free energy while regulated by the interfacial energy between the phases; the latter being intricately related to the interfacial curvatures. The resulting curvature topology promotes stretching-dominated deformation, which is stronger than bending-dominated deformation and, therefore, exhibits excellent mechanical resilience.[11,22] However, how to (in silico) tune the physics of spinodal decomposition to obtain tailored curvature topologies for favorable mechanics remains an open question.

A similar curvature design challenge is gaining attention in the field of bio-scaffolds and implants. Substrate curvatures play a significant role in inducing spatiotemporal growth, differentiation, and migration of biological cells and tissues.[27–32] For example, metamaterials based on triply periodic minimal surfaces (TPMS) gained popularity in the design of bone implants as they were believed to mimic the zero mean curvature of trabecular bone and in turn, enhance the long-term compatibility. However, a recent study[5] has challenged this assumption, revealing that trabecular bone displays a complex curvature profile instead, with significant variations across patients and anatomical sites. This highlights the need to develop porous structures with tunable curvature topologies, not only for bone implants but also for cell scaffolds that can adapt to diverse patient- and (anatomical) site-specific contexts.

Despite a wide variety of explorations ranging from TPMS to spinodoid metamaterials, a more general and unified topology description of smooth porous microstructures remains to be investigated. In this direction, Song[33] recently proposed a unifying phase-field framework to generate tubular and membranous topologies with diverse curvature profiles. Similar to the canonical spinodal decomposition model,[34] topologies within this framework are obtained as optimizers (subject to constant volume restriction) of energy functionals parameterized based on principal curvatures of the phase-field interface. While this

Y. Guo, S. Sharma, S. Kumar
Department of Materials Science and Engineering
Delft University of Technology
Mekelweg 2, 2628CD Delft, Netherlands
E-mail: S.Sharma-7@tudelft.nl; Sid.Kumar@tudelft.nl

Y. Guo
School of Aerospace Engineering and Applied Mechanics
Tongji University
Shanghai 200092, China

The ORCID identification number(s) for the author(s) of this article can be found under https://doi.org/10.1002/aisy.202300789.
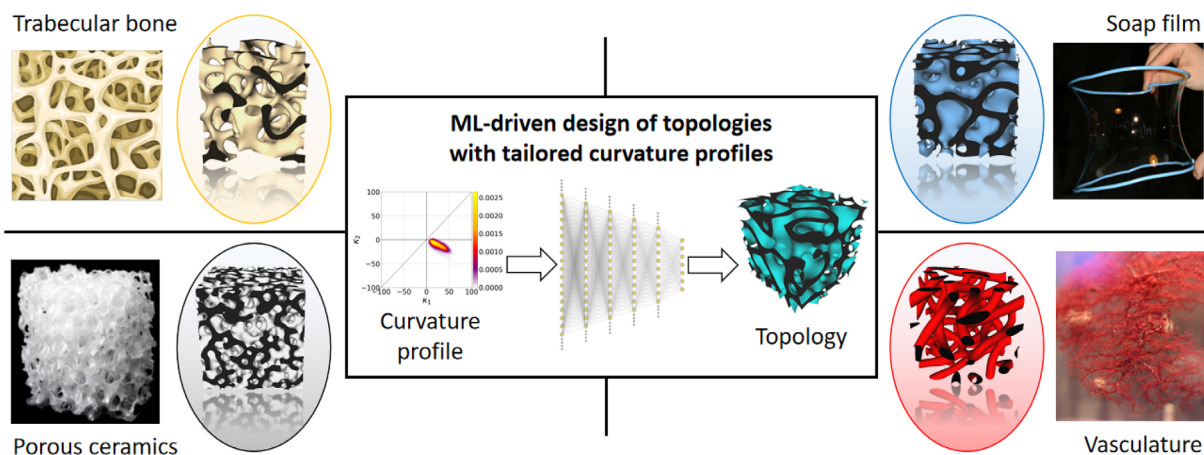
Figure 1. Natural materials and structures such as trabecular bone, soap films, porous ceramics, and vascular systems tend to have smooth curved topologies. Borrowing inspiration from those topologies, the ML-based inverse design framework provides a unified solution for on-demand rational design or mimicry of various smooth topologies with targeted curvature profiles. Since the curvature profile of a topology is directly related to its mechanical properties, this approach provides an efficient pathway to designing mechanical metamaterials with superior properties for applications in lightweight engineering materials, biomimetic structures, bio-implants, and more. Images adapted: trabecular bone by Laboratoires Servier, CC BY-SA 3.0, via Wikimedia Commons;[79] soap film by Blinking Spirit, CC0, via Wikimedia Commons;[80] porous ceramics by Onnovisser1979, CC BY-SA 3.0, via Wikimedia Commons;[81] vasculature by I'm in the garden, CC BY-SA 3.0, via Wikimedia Commons.[82]

approach opens up a design space to control curvature topology, key challenges persist. 1) Exploring the entire design–property space is nearly impossible because each topology requires a computationally expensive phase-field simulation. The characterization of the microstructural curvature profile by a high-dimensional probability distribution of principal curvatures further exacerbates the situation. 2) Although the curvature profile of a given topology is unique and simple to obtain, the inverse design, i.e., identifying a microstructural topology with a targeted curvature profile remains an open challenge. This is due to the ill-posedness of the inverse problem, i.e., multiple topologies with different design parameters may display the identical or similar curvature profiles, making it difficult to identify the optimal design. In addition, traditional design approaches such as topology optimization[35–37] and intuition-based approaches are not only computationally expensive, but they may also not be applicable to design for an unconventional target property, such as the microstructural curvature profile. To enhance the discovery of novel topologies, traditional empirical methods typically rely on collecting data from experiments or drawing inspiration from nature to mimic biological materials.[38–41] While intuition-based design approaches can be valuable, they often encounter limitations stemming from a restricted exploration of design possibilities. By relying solely on intuition, designers may overlook alternative perspectives and innovative solutions, leading to a narrower design space. For instance, while TPMS with varying Gaussian curvatures can be designed and fabricated,[42] the parameterization lacks generalizability to a broad and diverse range of smooth surfaces with tailored curvature profiles.

To overcome this limitation, a machine learning (ML) framework is introduced for generating smooth porous microstructures with inverse-designed curvature profiles (see Figure 1). By analyzing vast amounts of experimental and computational data, ML algorithms can bypass inefficient

trial-and-error methods and efficiently unravel hidden high-dimensional structure–property relations, leading to the design of novel materials with tailored properties. Employing a diverse array of ML techniques—from classical Bayesian optimization[43] to modern approaches such as variational autoencoders,[44] generative adversarial networks,[45] and diffusion models[46]—recent applications span a wide range of domains, including mechanical metamaterials,[22,47–51] composites,[52] photonics,[53] biomaterials,[54] and more. In the context of metamaterials and porous materials, while mechanical properties such as stiffness, Poisson's ratio, buckling modes, diffusivity, wave propagation, etc., have been inverse-designed, microstructural curvature as a design modality has not been explored.

To this end, we enable instant identification of microstructural topologies with precise targeted curvature profiles and unlock new possibilities in design of metamaterials and porous microstructures. This is achieved by strategically using a dual deep-neural-network (NN) setup[22,47,55] in tandem with a phase-field framework driven by curvature-based energetics[33] that bypasses both the aforementioned key challenges—namely, the computational bottleneck of phase-field methods and the ill-posedness in inverse design.

With the ability to generate tailored microstructural curvature profiles, we further investigate the interlink between curvature and mechanics. The membrane-flexural coupling appearing in the mechanics of shell/curved structures is strongly linked with their principal curvatures,[56] i.e., the redistribution of applied loads in the form of bending and stretching/compressive loads depends on the two principal curvatures of a curved surface. For a selection of micro-architectures with diverse curvature profiles, this load redistribution is studied by decomposing the stored strain energy into membrane and bending strain energies. Since a dominance of membrane deformation over bending deformation is known to promote higher mechanical resilience,

ADVANCED
SCIENCE NEWS

www.advancedsciencenews.com

ADVANCED
INTELLIGENT
SYSTEMS
Open Access

www.advintellsyst.com

the study of ratios of membrane to bending strain energies for diverse curvature profiles can guide the design of superior mechanical metamaterials through the presented inverse design approach.

In the following, we first introduce the design space and discuss the phase-field approach for topology generation. Subsequently, the ML framework for inverse design is introduced. Next, we demonstrate successful inverse design generalization for target curvatures beyond those in the training domain and show application to the design of topologies that mimic trabecular bone, spinodoid surfaces, and nodal surfaces. Lastly, mechanical aspects of the curvature-based microstructures are presented by investigating a set of topologies with diverse curvature profiles for their distribution of membrane and bending strain energies.

2. Results and Discussion

2.1. Design Space from Curvature-Based Energy Functional

We adopt the curvature-based phase-field framework of Song,[33] which makes it possible to unify topologies with spherical, tubular, and membranous features as well as their combinations with seamless transition. Briefly, for a given surface $\mathcal{S}$, let us consider an energy functional F based on the surface curvatures as

$$F[\mathcal{S}] = \int_{\mathcal{S}} f[S] \, \mathrm{d}S \quad \text{with}$$
$$f[S] = a_{20}\kappa_1^2 + a_{11}\kappa_1\kappa_2 + a_{02}\kappa_2^2 + a_{10}\kappa_1 + a_{01}\kappa_2 + a_{00} \tag{1}$$

where the integrand $f[S]$ (i.e., surface energy density) is a second-degree polynomial of the principal curvatures κ_1, κ_2 (by convention, $\kappa_1 \geq \kappa_2$) at the point S on the surface $\mathcal{S}$ and parameterized by the coefficients $\{a_{20}, a_{11}, a_{02}, a_{10}, a_{01}, a_{00}\}$. Similar to energy functional of the canonical Cahn–Hilliard equation,[22,34,57] minimizing this energy functional represents a compromise between minimizing the bending energy versus the surface area. The energy functional is minimized under constant volume constraint and periodic boundary conditions to yield diverse topologies. The energy minimization can be approximated by a phase-field model using a mass-preserving H^{-1} gradient flow of a two-phase system as

$$\dot{u} = \Delta \frac{\partial F_\varepsilon}{\partial u}(u) \quad \text{with} \quad m_0 = \frac{1}{|\Omega|} \int_\Omega u \, \mathrm{d}V \tag{2}$$

where $u:\Omega \to [-1, 1]$ denotes the phase field, i.e., a concentration field of one phase in the domain Ω. Without loss of generality, we assume a nondimensionalized domain $\Omega = [0, 100]^3$ (consequently, all subsequent length dimensions are normalized relative to the domain size). We assume the phase field contains diffused interfaces with a hyperbolic tangent profile and thickness length scale of $\varepsilon \ll 1$. F_ε is the corresponding phase-field approximation of F. m_0 denotes the constant volume constraint. u is initialized with random noise. After solving the gradient flow problem, the final surface $\mathcal{S}$ is extracted by applying the zero-level set on the resulting phase field. The zero-level set is not obtained exactly but rather approximated as a triangular surface mesh $\hat{\mathcal{S}}$ by

using the marching cubes algorithm.[58] **Figure 2**a shows a schematic of the topology generation process.

Within the phase-field approximation, we speak of diffused curvatures (or curvatures of diffused interfaces). Since the phase field u has a hyperbolic tangent profile, the diffused principal curvatures correspond precisely to the respective principal curvatures[59] at level sets of u. Detailed mathematical proof of phase-field approximation as well as implementation details can be found in ref. [33].

Let $\mathbf{\Theta} = (a_{20}, a_{11}, a_{02}, a_{10}, a_{01}, a_{00}, m_0)^\top$ be a vector of the design parameters that uniquely characterize the gradient flow and hence the topology generation. Note that the topologies are still stochastic due to the random initial conditions. Figure 2b shows a representative selection of diverse topologies and their corresponding curvature profiles obtained for different values of $\mathbf{\Theta}$.

For the curvature profile to be interpretable to the NN-based design algorithm, an encoding of the curvature profile is created for a given meshed surface $\hat{\mathcal{S}}$. The probability of $\hat{\mathcal{S}}$ containing the principal curvatures (κ_1, κ_2) is defined as

$$p(\kappa_1, \kappa_2 | \hat{\mathcal{S}}) = \frac{\sum_{i=1}^e \delta((\kappa_1, \kappa_2), (\hat{\kappa}_{1,i}, \hat{\kappa}_{2,i}))\hat{a}_i}{\sum_{i=1}^e \hat{a}_i} \tag{3}$$

where δ denotes the Kronecker delta, e is the total number of elements, and $\hat{a}_i$ and $(\hat{\kappa}_{1,i}, \hat{\kappa}_{2,i})$ denote the area and principal curvatures of the ith element in the mesh, respectively. Next, this probability distribution in $\kappa_1 - \kappa_2$ is discretized on a uniform grid of 200×200 bins (i.e., a 2D histogram) yielding a $[0, 1]^{200 \times 200}$ matrix encoding of the curvature profile. Note that this discrete probability matrix is lower triangular due to the convention of $\kappa_1 \geq \kappa_2$. To reduce the computational cost, the lower triangular part is serialized into a $k = 20,100$-dimensional encoding $\chi \in [0, 1]^k$, which is used in the downstream ML tasks.

2.2. Geometric Interpretation of the Design Space

The parameters $\{a_{20}, a_{11}, a_{02}, a_{10}, a_{01}, a_{00}\}$ in $\mathbf{\Theta}$ admit a characteristic geometric interpretation that directly correlates to the curvature profile of the resulting microstructure. The surface energy density in Equation (1) can be reformulated as a quadratic surface in the $\kappa_1 - \kappa_2 - f$ space such that

$$f[S] = g(\tilde{\boldsymbol{\kappa}}^\top \boldsymbol{M} \tilde{\boldsymbol{\kappa}} - c) \quad \text{with}$$
$$\tilde{\boldsymbol{\kappa}} = \underbrace{\begin{pmatrix} \cos\theta & \sin\theta \\ -\sin\theta & \cos\theta \end{pmatrix}}_{\text{rotation}} \underbrace{\begin{pmatrix} \kappa_1 - \kappa_1^c \\ \kappa_2 - \kappa_2^c \end{pmatrix}}_{\text{translation}} \quad \text{and} \tag{4}$$
$$\boldsymbol{M} = \underbrace{\begin{pmatrix} 1 & 0 \\ 0 & \alpha \end{pmatrix}}_{\text{aspect ratio}}$$

Here, $(\kappa_1^c, \kappa_2^c)^\top \in \mathbb{R}^2$, $\theta \in [-\pi/2, \pi/2)$, and $\alpha \in \mathbb{R}$ represent the translation, (counterclockwise) rotation, and aspect ratio in the $\kappa_1 - \kappa_2$ plane, respectively. The parameters $c \in \mathbb{R}$ and $g \in \mathbb{R}^+$ denote a vertical translation or bias along f and scaling factor, respectively; the latter does not affect the interrelations
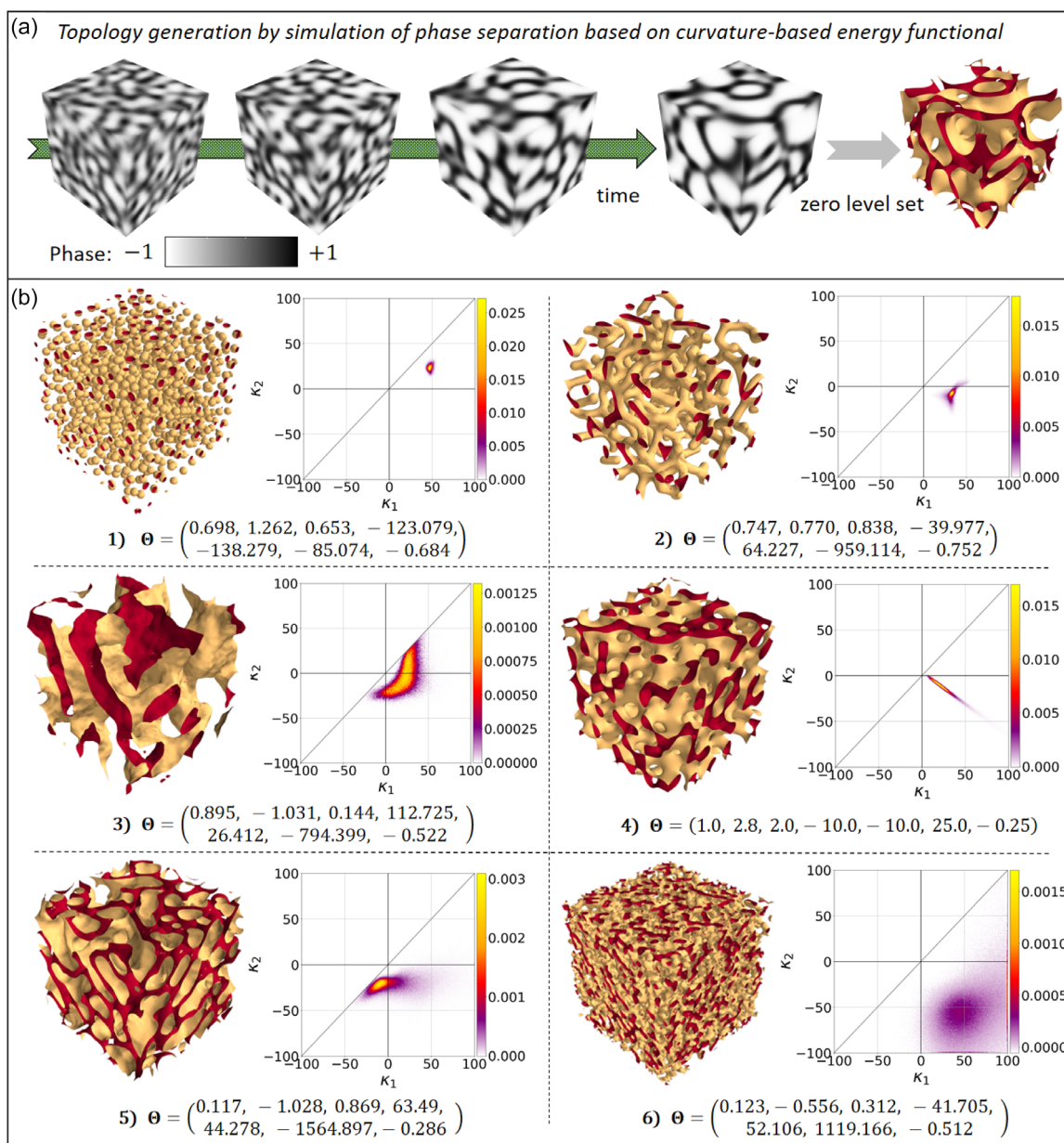
Figure 2. a) Schematic of topology generation using computationally expensive phase-field simulation based on curvature-driven energy functional. b) Representative selection of diverse topologies and their corresponding curvature profiles for different design parameters Θ. Typical microstructural features include spheres, tubules, or membranes. The curvature profile is visualized as the density scatter of the (surface) element-wise principal curvatures (κ_1 and κ_2); the density color of each scatter point is proportional to the cumulative surface area of the elements with similar principal curvatures in the mesh. Two elements are said to have similar principal curvatures if they lie in the same cell of a finely gridded κ_1–κ_2 plane.

between the individual curvature terms of the overall energy density. Section S1, Supporting Information, provides conversion formulas between the design parameters Θ and the equivalent geometrically interpretable ones, i.e., $\tilde{\Theta} = (\kappa_1^c, \kappa_2^c, \theta, \alpha, c, g, m_0)^\mathsf{T}$. In the cases when α is positive, zero, and negative, the quadratic surface is respectively an elliptic paraboloid, parabolic cylinder, and hyperbolic paraboloid, and consequently produce elliptic, linear, and hyperbolic contours on the κ_1–κ_2 plane. **Figure 3** illustrates how the combination

of rotation, translation, and aspect ratios yields a rich design space of surface energy densities.

The geometric interpretation of the surface energy density is reflected in the curvature profiles as the density plots are aligned with the contours of the quadratic surface of the surface energy density (see Figure 3 for representative examples). This is expected as the hot spots in the density plots qualitatively correspond to the regions of low surface energy density with respect to the principal curvatures.
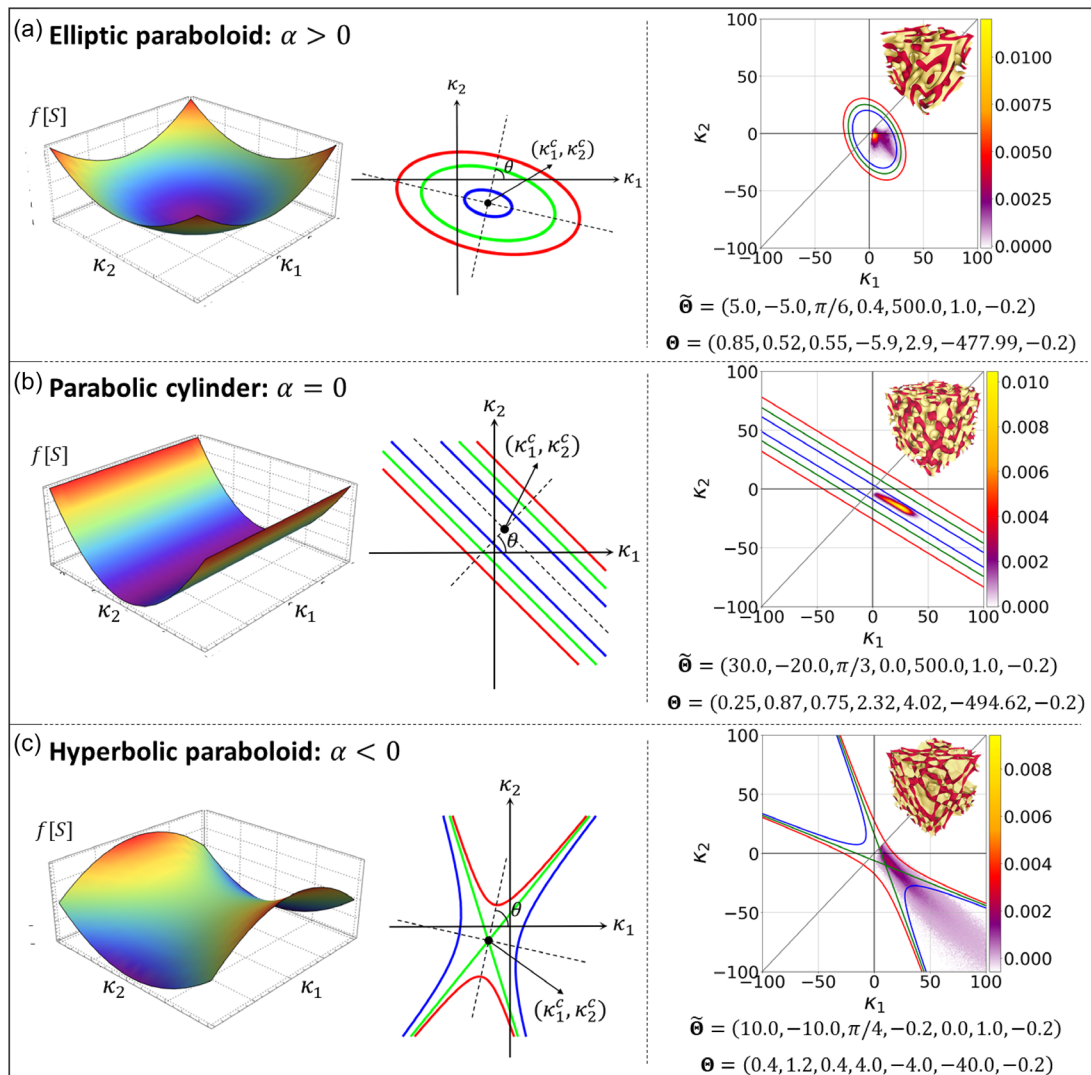
Figure 3. Geometric interpretation of the design space. For the cases when a) $\alpha > 0$, b) $\alpha = 0$, and c) $\alpha < 0$, the surface energy density $f[S]$ can be visualized as different kinds of quadratic surfaces (left column) and the corresponding contours (middle column) of $\kappa_1 - \kappa_2$. For each case, a representative example (right column) shows the qualitative correspondence between relevant contours of $f[S]$ and the resulting curvature profile.

2.3. Data-Driven Inverse Design

In light of the aforementioned relation between the design parameters and the curvature profile, we aim to invert this design–property space, i.e., identify the optimal Θ to achieve a target curvature profile. However, as discussed earlier, there are two key challenges: 1) the phase-field approach for topology generation is computationally expensive and therefore, a trial-and-error approach to inverse design is intractable; 2) the inverse design problem is ill-posed as multiple designs can have similar curvature profiles. To this end, we introduce a dual deep-NN setup (see **Figure 4**a for a schematic). A forward NN (f-NN) first surrogates the phase-field framework and maps the design parameters to the resulting microstructural curvature profile. An inverse NN (i-NN) then inverts the aforementioned design-to-curvature map and outputs the appropriate design

parameters (and corresponding phase-field energetics) required for a targeted curvature profile.

We start by creating a representative training dataset $\mathcal{D} = \{\{\Theta^{(i)}, \chi^{(i)}\}, i = 1, \ldots, n\}$ consisting of $n = 18,000$ pairs of design parameters Θ and the corresponding curvature profiles encoded as χ. Since the probability encodings can be sparse and skewed in distribution, independent nonlinear scaling is performed on the individual components of χ to enhance the sensitivity of the downstream ML approach. Section S2, Supporting Information, provides further details on the aforementioned data sampling and scaling strategy.

Let $\mathcal{F}_\omega : \mathbb{R}^7 \to \mathbb{R}^k$ denote an f-NN with a multilayer perceptron architecture parameterized by the set of trainable weights and biases ω. f-NN bypasses the phase-field evolution and directly maps the design parameters Θ to the curvature encoding $\chi = \mathcal{F}_\omega[\Theta]$. Since each design has a unique curvature profile
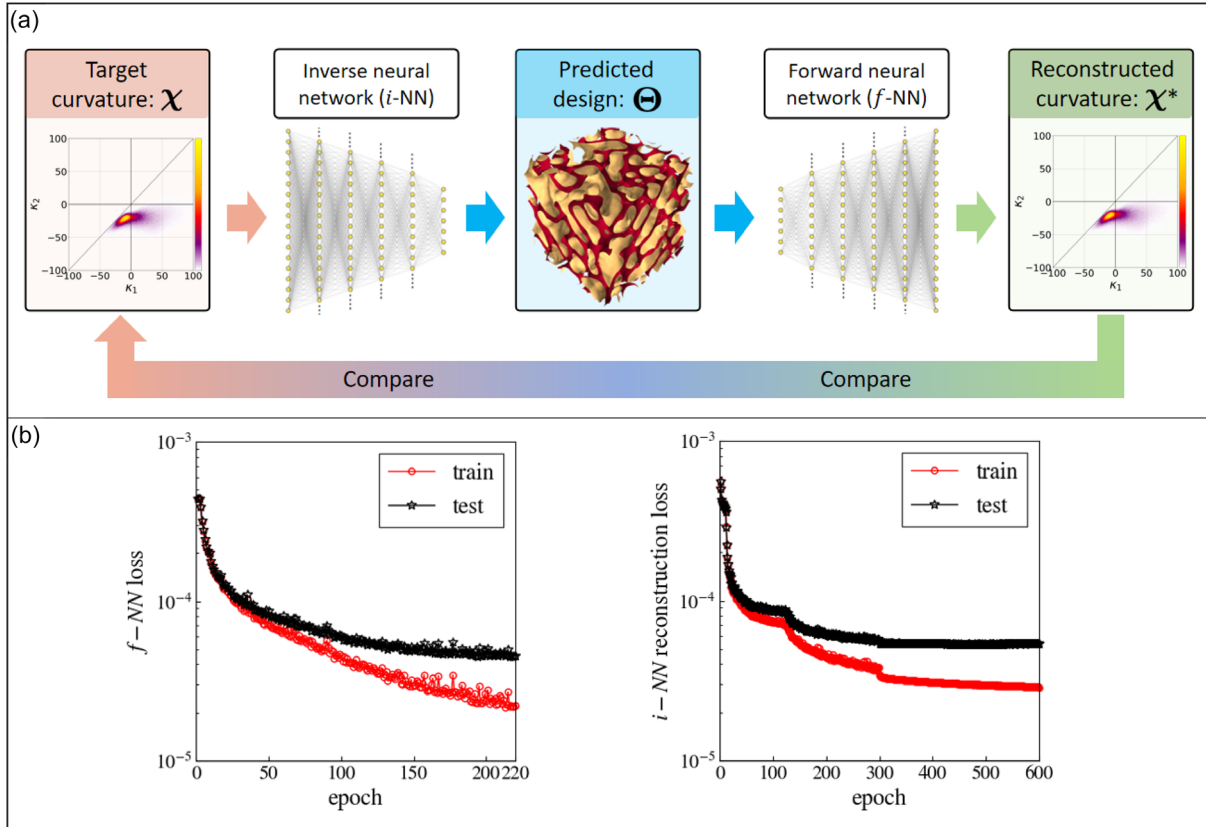
**ADVANCED
SCIENCE NEWS**

www.advancedsciencenews.com

**ADVANCED
INTELLIGENT
SYSTEMS**
Open Access

www.advintellsyst.com

Figure 4. a) Schematic of the ML-driven inverse design. For a target curvature encoding χ, the inverse model i-NN outputs the design parameters Θ. The pretrained forward model f-NN then bypasses the evolution of the phase field based on the energetics defined by Θ and directly reconstructs the curvature encoding χ^*. The difference between the target and reconstructed curvature encodings is then used to train the i-NN. b) Epoch-wise loss values (evaluated on the training and test datasets separately) during iterative training of the f-NN and i-NN.

(in the sense of averaging across the stochastic effects in topology generation), the forward problem is well-posed. Therefore, we train the f-NN by minimizing (mean squared error) the loss between the true and predicted curvature encodings with respect to the f-NN-parameters ω, i.e.

$$\mathcal{F}_\omega \leftarrow \min_\omega \frac{1}{n} \sum_{i=1}^n \|\mathcal{F}_\omega[\Theta^{(i)}] - \chi^{(i)}\|^2 \qquad (5)$$

We now tackle the inverse challenge. Let $\mathcal{G}_\tau : \mathbb{R}^k \to \mathbb{R}^7$ denote an i-NN with a multilayer perceptron architecture parameterized by the set of trainable weights and biases τ. The i-NN maps an input target curvature encoding χ to the design parameters $\Theta = \mathcal{G}_\tau[\chi]$. However, unlike the f-NN, a training strategy analogous to (5) fails due to the ill-posedness of the inverse problem. E.g., a high value of the naive loss $\|\mathcal{G}_\tau[\chi] - \Theta\|^2$ may indicate that the design parameters predicted by the i-NN and the ones from the dataset are different but does not hint anything about the possibility that these dissimilar designs may have similar curvature profiles. To counter this issue, we train the i-NN against the pretrained f-NN as

$$\mathcal{G}_\tau \leftarrow \min_\tau \frac{1}{n} \sum_{i=1}^n \|\mathcal{F}_\omega[\mathcal{G}_\tau[\chi^{(i)}]] - \chi^{(i)}\|^2. \qquad (6)$$

For the design predicted by the i-NN, i.e., $\mathcal{G}_\tau[\chi^{(i)}]$, the f-NN reconstructs the curvature encoding $\chi^* = \mathcal{F}_\omega[\mathcal{G}_\tau[\chi^{(i)}]]$; the loss of χ^* relative to the target χ from the dataset is minimized with respect to the i-NN parameters τ. The advantage of this loss function and training strategy over the naive approach is demonstrated later and in Section S3, Supporting Information. Note that the ML model is independent of the resolution and scale of the structure, as it takes the probability distribution of the point-wise surface curvatures (referred to as curvature encodings) as its input and outputs the design parameters for the phase-field model.

Both NNs are trained using gradient-based optimization. During i-NN training, the f-NN not only surrogates the computationally expensive phase-field evolution for curvature reconstruction, but also provides a differentiable map between Θ and χ. This differentiability is critical to computing the gradient $\partial \mathcal{F}_\omega / \partial \Theta$, which is in turn required for computing the sensitivity of the loss function in Equation (6) with respect to the i-NN parameters τ during training. Section S3, Supporting Information, provides additional implementation details as well as computational costs associated with both the NNs.

To evaluate the performance of the inverse design framework, we create an additional test dataset of 2000 design parameters and curvature encoding pairs, previously not seen by either of the NNs during training. Figure 4b shows that both f-NN and

ADVANCED
SCIENCE NEWS

www.advancedsciencenews.com

ADVANCED
INTELLIGENT
SYSTEMS
Open Access

www.advintellsyst.com

i-NN achieve high accuracy (indicated by the low loss values) across both training and test datasets without the presence of any under-/overfitting. A gallery of 21 representative examples in **Figure 5** shows exceptional agreement in the target curvature profiles versus the curvature profiles of the designs predicted by the *i*-NN, thereby providing qualitative evidence of the accuracy of the inverse design approach. **Figure 6** shows three additional examples along with a comparison of the design parameters Θ (and the resulting topology) in the dataset and the ones predicted by the *i*-NN. While the target and reconstructed curvature profiles are in agreement with each other, the design parameters are significantly different. It is further pronounced in the expectedly poor correlation between the true design parameters of the test dataset and the predicted design parameters from the *i*-NN; see Section S3 and Figure S4, Supporting Information. This verifies the ill-posedness of the inverse problem (i.e., multiple designs

parameters can lead to similar curvature profiles) and the advantage of the *i*-NN training strategy presented in Equation (6).

2.4. Generalization beyond the Training Space

To demonstrate the generalization ability of our approach, we inverse design the topologies for tailored curvature profiles that are representative of three different (meta-)material/structural classes.

2.4.1. Benchmark 1: Trabecular Bone

Recent works[31,42] have shown the important role of substrate curvature in growth of bone cells on additively manufactured implants. Motivated by this, we target the microstructural
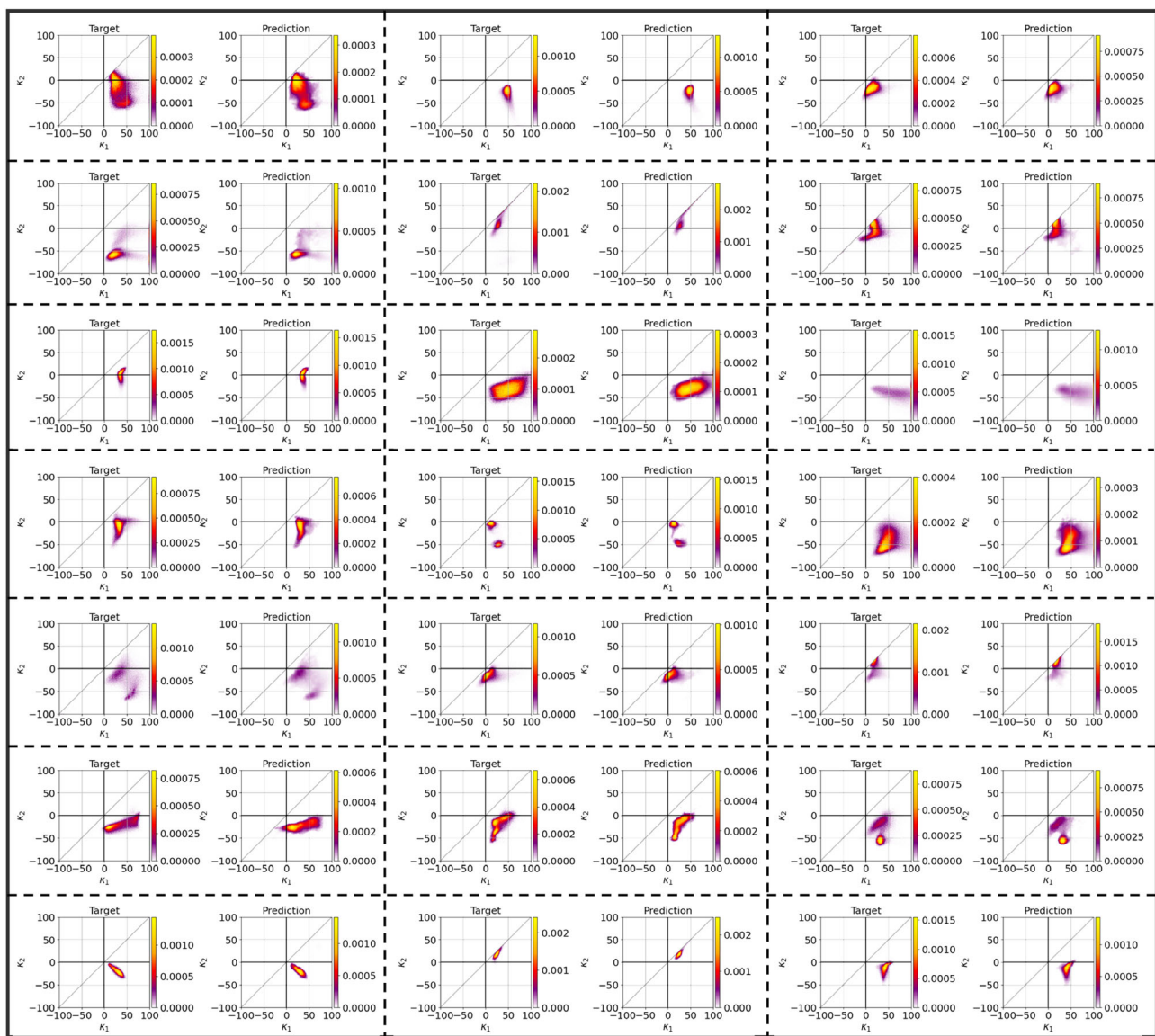

Figure 5. A gallery of representative examples of targeted curvature profiles from the previously unseen test dataset versus curvature profiles of the topologies predicted by the *i*-NN.
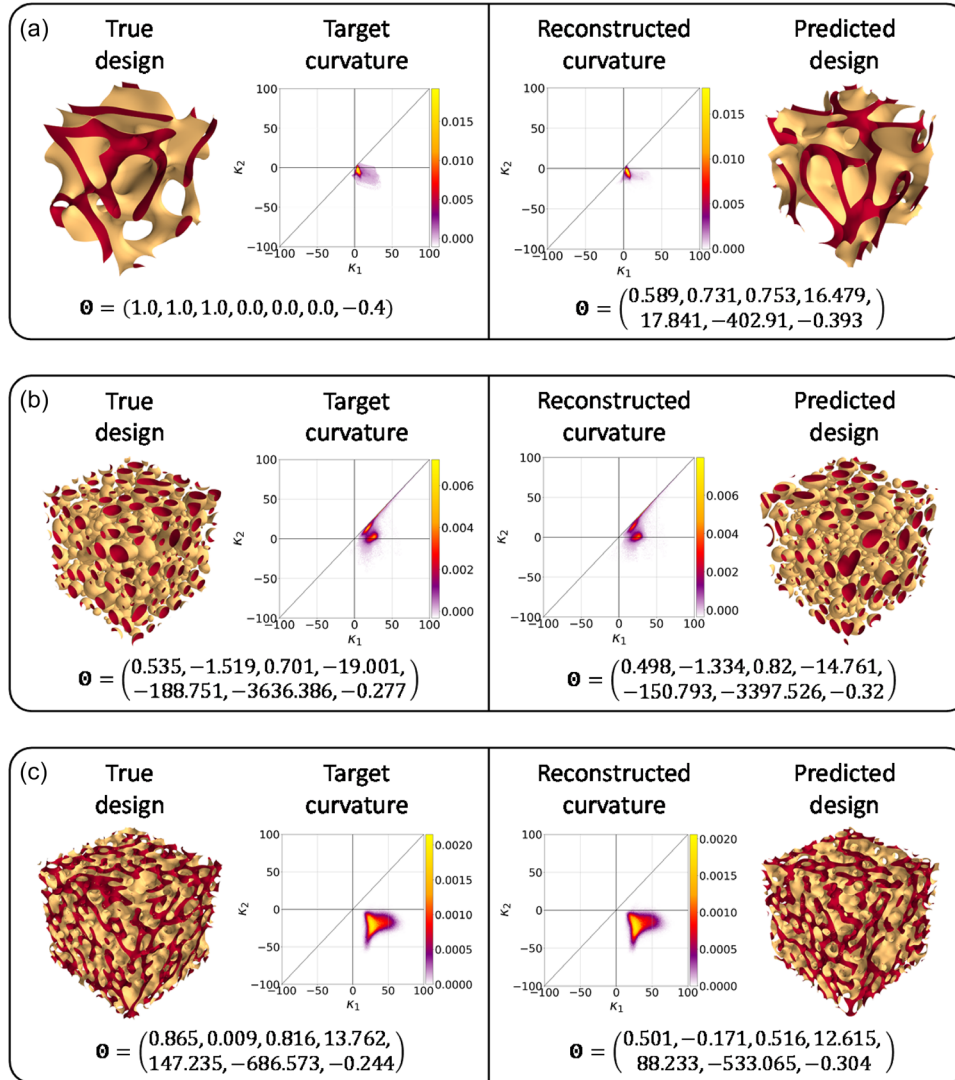
Figure 6. Comparisons between the design parameters Θ (and the resulting topologies) and the ones predicted by the *i*-NN for three representative examples a,b), and c) from the dataset.

topology of bone to benchmark our inverse design framework. Specifically, we consider a trabecular bone sample from Tozzi et al.[60] (see **Figure 7**a). The microstructural data is available as gray scale 3D-voxelated image obtained directly from micro-computed tomography. The surface representation of the trabecular bone sample is extracted by using an appropriate image processing and smoothing algorithm, the details of which are provided in Section S4, Supporting Information.

2.4.2. Benchmark 2: Spinodal Decomposition

Diffusion-driven spinodal decomposition in a binary phase system can produce complex and diverse topologies (which are also used in spinodoid metamaterials[22]). Here, we briefly review the formulation of topologies emergent from spinodal decomposition and refer to refs. [22,24] for details. The early stage of a spinodal decomposition process is mathematically described by a Gaussian random field, i.e., a linear superposition of $Q \gg 1$ standing waves:

$$\varphi(\boldsymbol{x}) = \sqrt{\frac{2}{Q}} \sum_{q=1}^{Q} \cos(\beta \boldsymbol{v}_q \cdot \boldsymbol{x} + \gamma_q) \tag{7}$$

where $\varphi : \Omega \to \mathbb{R}$ and $\beta > 0$ denote a phase field and a constant wavenumber, respectively; the latter determines the microstructural length scale of the former. $\boldsymbol{v}_q$ and γ_q denote, respectively, the wave vector and phase angle of qth standing wave and are randomly and uniformly sampled as

$$\boldsymbol{v}_q \sim \mathcal{U}\left(\left\{ \begin{array}{c} \boldsymbol{v} \in \mathrm{S}^2 : (|\boldsymbol{v} \cdot \hat{\boldsymbol{e}}_1| > \cos\theta_1) \oplus (|\boldsymbol{v} \cdot \hat{\boldsymbol{e}}_2| > \cos\theta_2) \\ \oplus (|\boldsymbol{v} \cdot \hat{\boldsymbol{e}}_3| > \cos\theta_3) \end{array} \right\}\right) \tag{8}$$

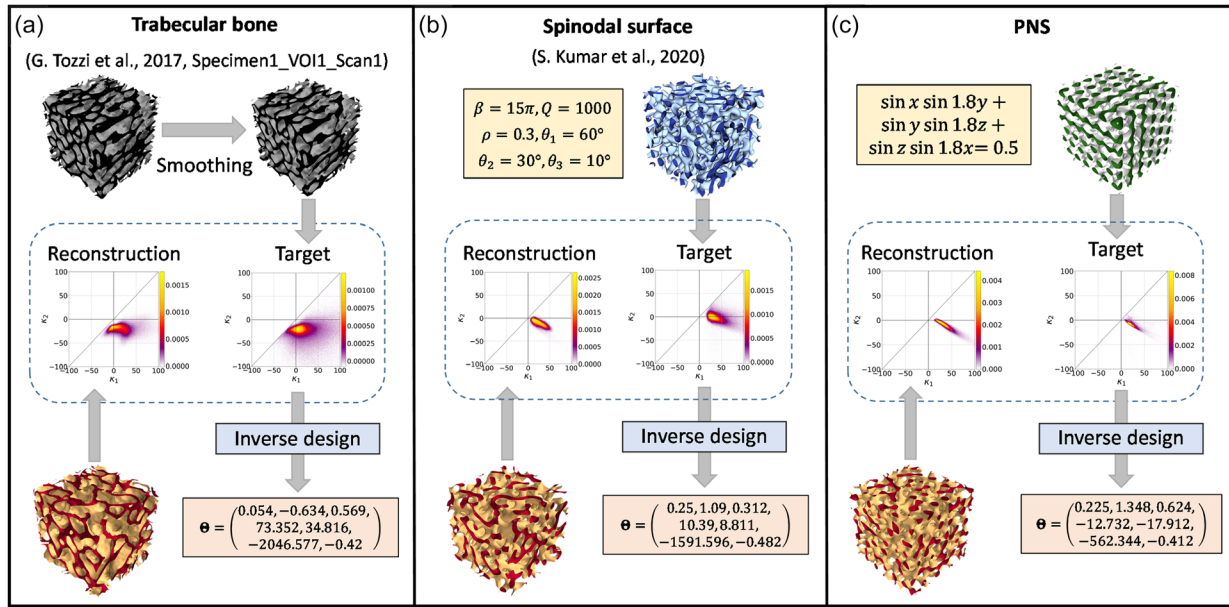$$\gamma_p \sim \mathcal{U}([0, 2\pi))$$

Figure 7. Curvature-based surface inverse design applications including a) a computed tomography scan of trabecular bone specimen taken from Tozzi et al.[60] b) spinodal surface created from six design parameters from Kumar et al.[22] and c) PNS surface governed by an implicit equation. The curvature profile of targeted structures are queried through the *i*-NN which outputs the design parameters Θ. The corresponding topology is then generated through the phase-field approach and the curvature profile is reconstructed for comparison with the original target. Additional benchmarks are presented in Section S5, Supporting Information.

where $\{e_1, e_2, e_3\}$ denote S^2 which is the set of all unit vectors. Parameters $\theta_1, \theta_2, \theta_3 \in [0, \pi/2)$ restrict the directional distribution of the wave vectors to respective angles from the Cartesian basis vectors. This parametric distribution is interpreted as anisotropic mobility along preferred directions during the spinodal decomposition process. The final topology is obtained by extracting the phase interface which is given by a level set as

$$\varphi = \sqrt{2}\,\text{erf}^{-1}(2\rho - 1), \tag{9}$$

where $\rho \in [0, 1]$ is the volume fraction of one of the phases. For the purpose of this benchmark, we generate a spinodoid topology (see Figure 7b) with $\beta = 15\pi$, $Q = 1000$, $\theta_1 = 60°$, $\theta_2 = 30°$, $\theta_3 = 10°$, and $\rho = 0.3$.

2.4.3. Benchmark 3: Periodic Nodal Surfaces

These are smooth implicit surfaces composed of Fourier series components[61,62] and are widely studied across different fields in mathematics,[63–65] chemistry,[61,66,67] mechanics,[68,69] and more. Periodic nodal surfaces (PNSs) are particularly popular as closed-form approximations of minimal surfaces (i.e., zero mean curvature) such as the famous Schwarz[70,71] and Schoen[72,73] surfaces. Since minimal surfaces present a curvature distribution ($\kappa_2 = -\kappa_1$) trivial for a benchmark, here we consider a non-minimal PNS given by

$$\sin(x)\sin(1.8y) + \sin(y)\sin(1.8z) + \sin(z)\sin(1.8x) = 0.5 \tag{10}$$

and visualized in Figure 7c.

Across all three benchmarks, we scale the topologies to the same domain size as Ω and extract the curvature profile which is passed as a design target to the *i*-NN. For each benchmark, the *i*-NN successfully predicts a topology with a curvature profile that closely matches the target (see Figure 7 and Section S5, Supporting Information). Remarkably, the *i*-NN achieves this despite no prior information about trabecular bone, spinodal decomposition, or PNS topologies during the training stage and indicates excellent generalization well beyond the scope of the training dataset. The *i*-NN is also able to design for similar curvature profiles despite key geometrical differences such as periodicity (in the PNS benchmark) and anisotropy (in all three benchmarks) in the target, which highlights further the ill-posedness of the inverse design challenge and the benefit of the proposed approach. In addition, the generalization capability is particularly useful for biomimetic implants and scaffolds where large training datasets (of, e.g., bone) are particularly scarce, and small amounts of patient-/site-specific data can be used for fine-tuning or transfer learning of the pretrained *i*-NN for improved accuracy.

2.5. Curvature Determines Mechanics

For slender structures—both natural (e.g., skull, egg shells, sea shells) and man-made (e.g., aircraft fuselage, pressure vessels, domes)—curved geometries are preferred as structural elements over flat ones due to their ability to redistribute applied loads into the stronger in-plane stretching-dominated behavior as opposed to the weaker out-of-plane bending-dominated behavior.[11] In the light of microstructures with tailorable curvature profiles,
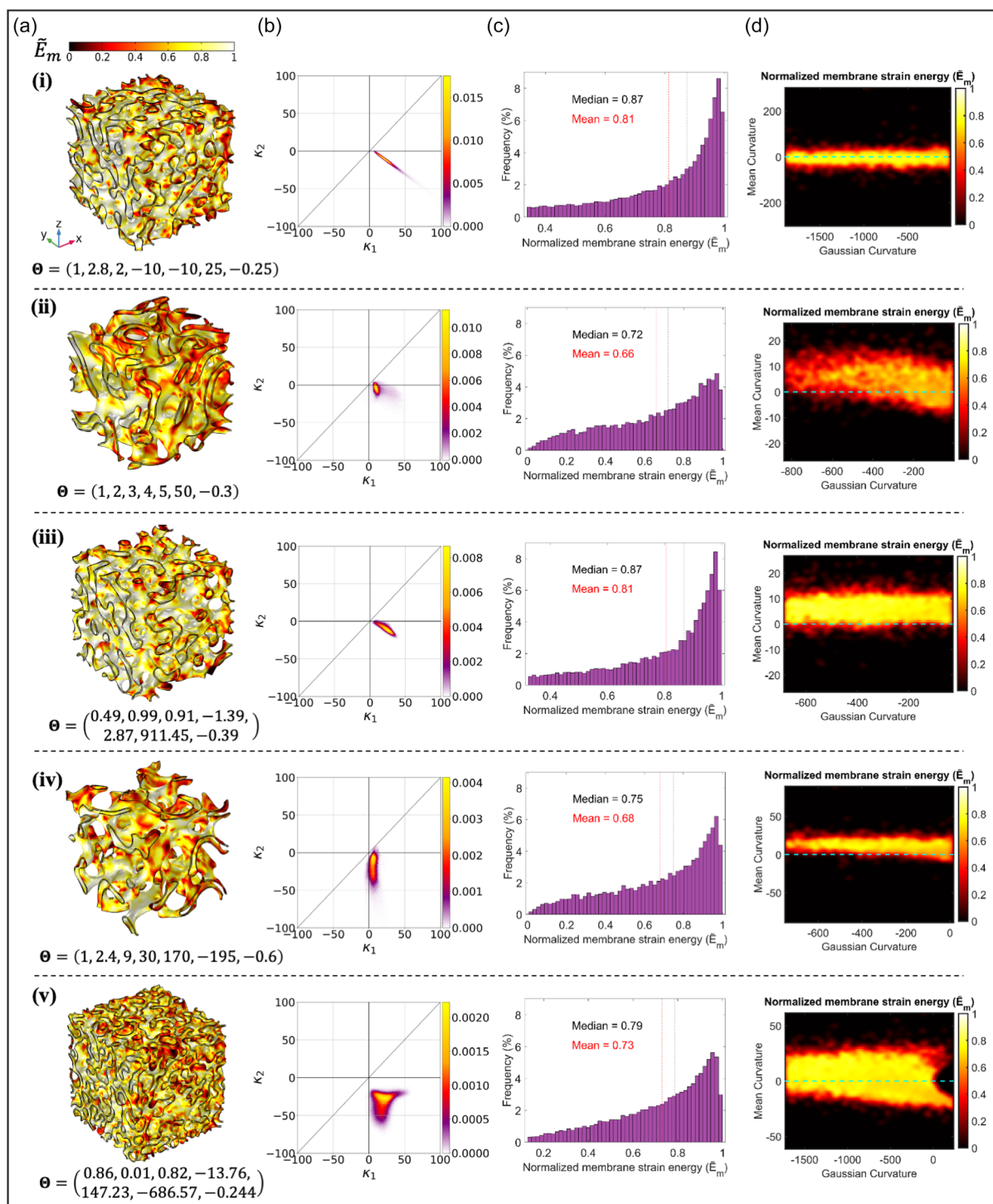
Figure 8. Interplay of membrane and bending strain energies in diverse inverse-designed shellular topologies (numbered (i)–(v)) under unit tensile load. a) Distribution of normalized membrane strain energy $\tilde{E}_m$ in the topologies and b) their corresponding curvature profiles. c) Distribution of $\tilde{E}_m$ over the surface area of each topology. Topologies with close-to-zero mean curvature ((i) and (iii)) show relatively higher values of $\tilde{E}_m$, indicating a stretching-dominated behavior. d) Distribution of mean and Gaussian curvatures; colored by the mean of $\tilde{E}_m$ for the corresponding curvature values found within a topology. Higher $\tilde{E}_m$ (i.e., stretching-dominated deformation) is observed in the proximity of zero mean curvature (dashed cyan line) compared to other curvatures.

we explore this interplay between curvature and mechanics across our design space.

Specifically, we consider five representative topologies with diverse curvature profiles (see **Figure 8**) obtained from the inverse design strategy. Each topology is modeled as a shellular structure with the shell thickness equal to 1% of the domain length (recall $\Omega = [0, 100]^3$) and made of a linearly elastic material with Poisson's ratio of 0.3 and a unit Young's modulus. Note that we restrict ourselves to curvature distributions that admit bicontinuous topologies only as it would be physically required for a self-standing shellular structure. We perform finite-element analysis of the shellular structure undergoing quasi-static uniaxial tension, using six degrees of freedom quadratic shell elements with the mixed interpolation of tensorial components (MITC) formulation.[74] The choice of Young's modulus and applied load are arbitrary as they do not affect the following analysis.

For each case, we investigate the distribution of the total in-plane membrane strain energy E_m and out-of-plane bending strain energy E_b (obtained by summing over the membrane and bending strain energies of all the shell elements, respectively). Figure 8a shows the spatial distribution of the normalized membrane strain energy, i.e., $\tilde{E}_m = E_m/(E_m + E_b)$, with $\tilde{E}_m = 1$ and $\tilde{E}_m = 0$ denoting pure stretching- and bending-dominated deformations respectively. In Figure 8b,c, the topologies with curvature distribution closer to zero mean curvature (first and third row) show higher mean and median in the distribution of $\tilde{E}_m$, relative to the others, indicating higher stretching-dominated deformation. Figure 8d further shows the distribution of element-wise $\tilde{E}_m$ with respect to the mean and Gaussian curvature. Notably, elements with or close to zero mean curvature predominantly store stretching-dominated energy, which largely corroborates the beneficial mechanical properties of TPMS observed across several prior works.[75–77] Moreover, a similar study is conducted under a shear load in Section S5, Supporting Information, which shows that the distribution of strain energy between membrane and bending modes follows the same correlation with curvature profile under varying loading conditions.

3. Conclusion

The presented framework enables inverse design of smooth topologies with tailored curvature profiles. This is achieved by training a dual deep-NN setup to surrogate a phase field driven by a curvature-based energy functional and then invert the process. Our approach provides excellent generalization beyond both the design space as well as the space of the training data—as evidenced by successful reconstruction of curvature of topologies from different data sources, including microtomography of trabecular bone, spinodal surfaces, and implicit nodal surfaces. Notably, the ML framework achieves accurate reconstructions without any prior knowledge about these structures and their symmetries during the learning phase. Linking with mechanics, the analysis of strain energy distribution reveals a correlation between curvature profile and stretching versus bending dominated deformations, which can be exploited for tailoring the topology for improved mechanical resilience. Overall, our framework unlocks curvature as a new design modality with

applications in mechanical metamaterials and bio-scaffolds/implants.

Future directions of interest may include incorporating anisotropic and higher-order curvature descriptors for a more generalizable design space and integrating topology curvature with nonlinear mechanical response in inverse design. Specifically, two surfaces can have similar curvature distributions, yet the orientation distribution of those surfaces can be significantly different. Higher-order curvature descriptors such as Minkowski functionals[78] can be introduced in the energetics of the phase-field methods to preferentially bias both surface curvature and orientation distributions simultaneously. This will expand the design space to include anisotropic designs, and can be relevant for controllable anisotropy in mechanical response of metamaterials as well as mimicking topological anisotropy in bio-scaffolds for improved bio-compatibility. Additionally, the incorporation of spatially varying design parameters will facilitate the creation of topologies with spatially graded curvature variation (commonly observed in biological tissues and bones), offering the potential for a more comprehensive modeling approach.

Conflict of Interest

The authors declare no conflict of interest.

Author Contributions

Y.G.: developed and implemented the inverse design algorithm and performed numerical experiments. S.S.: performed the mechanics simulations and analyzed the results. S.K.: conceived the research. S.S. and S.K.: supervised the research. All the authors wrote and approved the final manuscript.

Data Availability Statement

The datasets and codes generated during the current study are available at https://github.com/mmc-group/inverse-designed-surface-curvatures.

ADVANCED
SCIENCE NEWS

www.advancedsciencenews.com

ADVANCED
INTELLIGENT
SYSTEMS
Open Access

www.advintellsyst.com

[1] J. E. Taylor, *Ann. Math.* **1976**, *103*, 489.

[2] F. J. Almgren, J. E. Taylor, *Sci. Am.* **1976**, *235*, 82.

[3] A. M. Turing, *Philos. Trans. R. Soc. London, Ser. B* **1952**, *237*, 37.

[4] S. Kondo, *J. Theor. Biol.* **2017**, *414*, 120.

[5] S. J. Callens, D. C. Tourolle né Betts, R. Müller, A. A. Zadpoor, *Acta Biomater.* **2021**, *130*, 343.

[6] M. Ralph, *Nat. Rev. Rheumatol.* **2009**, *5*, 373.

[7] M. Puhka, M. Joensuu, H. Vihinen, I. Belevich, E. Jokitalo, *Mol. Biol. Cell* **2012**, *23*, 2424.

[8] S. K. Ramasamy, *Stem Cells Int.* **2017**, *2017*.

[9] K. K. Sivaraj, R. H. Adams, *Development* **2016**, *143*, 2706.

[10] J. Erlebacher, M. J. Aziz, A. Karma, N. Dimitrov, K. Sieradzki, *Nature* **2001**, *410*, 450.

[11] C. M. Portela, A. Vidyasagar, S. Krödel, T. Weissenbach, D. W. Yee, J. R. Greer, D. M. Kochmann, *Proc. Natl. Acad. Sci.* **2020**, *117*, 5686.

[12] J. D. Hill, P. C. Millett, *Macromolecules* **2019**, *52*, 9495.

[13] D. S. Jung, J. Bang, T. W. Park, S. H. Lee, Y. K. Jung, M. Byun, Y.-R. Cho, K. H. Kim, G. H. Seong, W. I. Park, *Nanoscale* **2019**, *11*, 18559.

[14] J. Ren, C. Zhou, X. Chen, M. Dolejsi, G. S. W. Craig, P. A. Rincon Delgadillo, T. Segal-Peretz, P. F. Nealey, *ACS Appl. Mater. Interfaces* **2018**, *10*, 23414.

[15] P. Castillo, S. Gómez, *Appl. Math. Comput.* **2021**, *397*, 125984.

[16] M. Jiang, J. Zhang, J. Zhu, X. Yu, L. Bevilacqua, *Comput. Methods Appl. Mech. Eng.* **2021**, *381*, 113806.

[17] R. Anzaki, S.-I. Ito, H. Nagao, M. Mizumaki, M. Okada, I. Akai, *Phys. Rev. B* **2021**, *103*, 094408.

[18] J. Diaz, M. Pinna, A. V. Zvelindovsky, I. Pagonabarraga, *Adv. Theor. Simul.* **2022**, *5*, 2100433.

[19] V. Ankudinov, P. K. Galenko, *Philos. Trans. R. Soc., A* **2022**, *380*, 20200318.

[20] C. Soyarslan, S. Bargmann, M. Pradas, J. Weissmüller, *Acta Mater.* **2018**, *149*, 326.

[21] M.-T. Hsieh, B. Endo, Y. Zhang, J. Bauer, L. Valdevit, *J. Mech. Phys. Solids* **2019**, *125*, 401.

[22] S. Kumar, S. Tan, L. Zheng, D. M. Kochmann, *npj Comput. Mater.* **2020**, *6*, 73.

[23] M.-T. Hsieh, M. R. Begley, L. Valdevit, *Mater. Des.* **2021**, *207*, 109838.

[24] L. Zheng, S. Kumar, D. M. Kochmann, *Comput. Methods Appl. Mech. Eng.* **2021**, *383*, 113894.

[25] A. G. Izard, J. Bauer, C. Crook, V. Turlo, L. Valdevit, *Small* **2019**, *15*, 1903834.

[26] M. Röding, V. W. Skärström, N. Lorén, *Sci. Rep.* **2022**, *12*, 17413.

[27] Y. Lou, J.-F. Rupprecht, S. Theis, T. Hiraiwa, T. E. Saunders, *Phys. Rev. Lett.* **2023**, *130*, 108401.

[28] M. Werner, S. B. G. Blanquer, S. P. Haimi, G. Korus, J. W. C. Dunlop, G. N. Duda, D. W. Grijpma, A. Petersen, *Adv. Sci.* **2016**, *4*, 600347.

[29] A. A. Zadpoor, *Biomater. Sci.* **2015**, *3*, 231.

[30] Y. Zhang, P. Wang, J. Jin, L. Li, S.-Y. He, P. Zhou, Q. Jiang, C. Wen, *Biotechnol. Bioeng.* **2022**, *119*, 591.

[31] S. J. Callens, R. J. Uyttendaele, L. E. Fratila-Apachitei, A. A. Zadpoor, *Biomaterials* **2020**, *232*, 119739.

[32] S. J. P. Callens, D. Fan, I. A. J. van Hengel, M. Minneboo, P. J. Diaz-Payno, M. M. Stevens, L. E. Fratila-Apachitei, A. A. Zadpoor, *Nat. Commun.* **2023**, *14*, 855.

[33] A. Song, *J. Math. Imaging Vision* **2021**, *64*, 17.

[34] J. W. Cahn, J. E. Hilliard, *J. Chem. Phys.* **1958**, *28*, 258.

[35] O. Sigmund, K. Maute, *Struct. Multidiscip. Optim.* **2013**, *48*, 1031.

[36] X. Zhai, W. Wang, F. Chen, J. Wu, *Comput. Methods Appl. Mech. Eng.* **2024**, *418*, 116530.

[37] J. Gao, M. Xiao, Y. Zhang, L. Gao, *Chin. J. Mech. Eng.* **2020**, *33*, 87.

[38] L. J. Gibson, M. F. Ashby, B. A. Harley, *Cellular Materials in Nature and Medicine*, Cambridge University Press, Cambridge **2010**.

[39] H. D. Espinosa, A. L. Juster, F. J. Latourte, O. Y. Loh, D. Gregoire, P. D. Zavattieri, *Nat. Commun.* **2011**, *2*, 173.

[40] F. Barthelat, H. Espinosa, *Exp. Mech.* **2007**, *47*, 311.

[41] F. Barthelat, R. Rabiei, *J. Mech. Phys. Solids* **2011**, *59*, 829.

[42] Y. Yang, T. Xu, H.-P. Bei, L. Zhang, C.-Y. Tang, M. Zhang, C. Xu, L. Bian, K. W.-K. Yeung, J. Y. H. Fuh, X. Zhao, *Proc. Natl. Acad. Sci.* **2022**, *119*, e2206684119.

[43] R. Garnett, *Bayesian Optimization*, Cambridge University Press, Cambridge **2023**.

[44] L. P. Cinelli, M. A. Marins, E. A. B. da Silva, S. L. Netto, *Variational Methods for Machine Learning with Applications to Deep Networks*, Springer International Publishing, Cham **2021**, pp. 111–149.

[45] *Advances in Neural Information Processing Systems-*, Vol. *27* (Eds: I. Goodfellow, J. Pouget-Abadie, M. Mirza, B. Xu, D. Warde-Farley, S. Ozair, A. Courville, Y. Bengio, In Z. Ghahramani, M. Welling, C. Cortes, N. Lawrence, K. Weinberger), Curran Associates, Inc. **2014**.

[46] L. Yang, Z. Zhang, Y. Song, S. Hong, R. Xu, Y. Zhao, W. Zhang, B. Cui, M.-H. Yang, *ACM Comput. Surv.* **2023** *56*, 1.

[47] J.-H. Bastek, S. Kumar, B. Telgen, R. N. Glaesener, D. M. Kochmann, *Proc. Natl. Acad. Sci.* **2021**, *119*, 1.

[48] L. Wang, Y.-C. Chan, F. Ahmed, Z. Liu, P. Zhu, W. Chen, *Comput. Methods Appl. Mech. Eng.* **2020**, *372*, 113377.

[49] M. A. Bessa, P. Glowacki, M. Houlder, *Adv. Mater.* **2019**, *31*, 1904845.

[50] N. N. Vlassis, W. Sun, *Comput. Methods Appl. Eng.* **2023** *413*, 116126.

[51] Y. Mao, Q. He, X. Zhao, *Sci. Adv.* **2020**, *6*, 17.

[52] G. X. Gu, C.-T. Chen, M. J. Buehler, *Extreme Mech. Lett.* **2018**, *18*, 19.

[53] I. Malkiel, M. Mrejen, A. Nagler, U. Arieli, L. Wolf, H. Suchowski, *Light: Sci. Appl.* **2018**, *7*, 1.

[54] A. Suwardi, F. Wang, K. Xue, M.-Y. Han, P. Teo, P. Wang, S. Wang, Y. Liu, E. Ye, Z. Li, X. J. Loh, *Adv. Mater.* **2021**, *34*, 2102703.

[55] S. Van 't Sant, P. Thakolkaran, J. Martínez, S. Kumar, *Mech. Mater.* **2023**, *182*, 104668.

[56] J. N. Reddy, *Theory and Analysis of Elastic Plates and Shells*, CRC Press, Boca Raton **2006**.

[57] A. Vidyasagar, S. Krödel, D. M. Kochmann, *Proc. R. Soc. A* **2018**, *474*, 20180535.

[58] W. E. Lorensen, H. E. Cline, *SIGGRAPH Comput. Graph.* **1987**, *21*, 163.

[59] R. Goldman, *Comput. Aided Geom. Des.* **2005**, *22*, 632, geometric Modelling and Differential Geometry.

[60] G. Tozzi, E. Dall'Ara, M. Palanca, M. Curto, F. Innocente, L. Cristofolini, *J. Mech. Behav. Biomed. Mater.* **2017**, *67*, 117.

[61] S. Leoni, *Ph.D. Thesis*, ETH Zurich, **1998**.

[62] P. J. Gandy, S. Bardhan, A. L. Mackay, J. Klinowski, *Chem. Phys. Lett.* **2001**, *336*, 187.

[63] H. Karcher, K. Polthier, *Philos. Trans. R. Soc., A* **1996**, *354*, 2077.

[64] W. H. Meeks III, *Indiana Univ. Math. J.* **1990**, *39*, 877.

[65] S.-D. Yang, H. G. Lee, J. Kim, *Comput. Phys. Commun.* **2010**, *181*, 1037.

[66] R. Nesper, S. Leoni, *ChemPhysChem* **2001**, *2*, 413.

[67] F. M. Baena-Moreno, M. Gonzalez-Castano, J. C. Navarro de Miguel, K. U. Miah, R. Ossenbrink, J. A. Odriozola, H. Arellano-Garcia, *ACS Sustainable Chem. Eng.* **2021**, *9*, 8198.

[68] S. C. Kapfer, S. T. Hyde, K. Mecke, C. H. Arns, G. E. Schröder-Turk, *Biomaterials* **2011**, *32*, 6875.

[69] C. Bonatti, D. Mohr, *J. Mech. Phys. Solids* **2019**, *122*, 1.

[70] M. Ross, *Differ. Geom. Appl.* **1992**, *2*, 179.

[71] X. Guo, J. Ding, X. Li, S. Qu, X. Song, J. Y. H. Fuh, W. F. Lu, W. Zhai, *Int. J. Mech. Sci.* **2022**, *216*, 106977.

[72] C. Ciliberto, M. M. Lopes, X. Roulleau, *Comment. Math. Helv.* **2015**, *90*, 59.

[73] C. Rito, X. Roulleau, A. Sarti, arXiv preprint arXiv:1609.02235 **2016**.

[74] K.-J. Bathe, E. N. Dvorkin, *Int. J. Numer. Methods Eng.* **1986**, *22*, 697.

[75] V. Shevchenko, S. Balabanov, M. Sychov, L. Karimova, *ACS Omega* **2023**, *8*, 26895.

[76] I. Maskery, L. Sturm, A. Aremu, A. Panesar, C. Williams, C. Tuck, R. Wildman, I. Ashcroft, R. Hague, *Polymer* **2018**, *152*, 62, sI: Advanced Polymers for 3DPrinting/Additive Manufacturing.

[77] N. Qiu, Y. Wan, Y. Shen, J. Fang, *Int. J. Mech. Sci.* **2023**, *261*, 108657.

[78] G. E. Schröder-Turk, W. Mickel, S. C. Kapfer, M. A. Klatt, F. M. Schaller, M. J. F. Hoffmann, N. Kleppmann, P. Armstrong, A. Inayat, D. Hug, M. Reichelsdorfer, W. Peukert, W. Schwieger, K. Mecke, *Adv. Mater.* **2011**, *23*, 2535.

[79] Laboratoires Servier, Spongy Bone Wikimedia Commons, https://commons.wikimedia.org/wiki/File:Spongy_bone_-_Trabecular_bone_-_Normal_trabecular_bone_--_Smart-Servier.png (accessed: September 2023).

[80] Blinking Spirit, Photo of a Soap Bubble Creating a Catenoid, Wikimedia Commons, https://commons.wikimedia.org/wiki/File:Bulle_cat%C3%A9no%C3%AFde.png (accessed: September 2023).

[81] Onnovisser1979, Photo of Porous Ceramic Granule, Photo Shot by Michel Porro, Wikimedia Commons, https://commons.wikimedia.org/wiki/File:Cam_Bioceramics_Large_Porous_Granule.png (accessed: September 2023).

[82] I'm in the Garden, Injection Preparation; Universum Bremen, Wikimedia Commons, https://commons.wikimedia.org/wiki/File:Blutgef%C3%A4%C3%9Fe_0387.JPG (accessed: September 2023).